# Influence of Following, Regular, and Irregular Long Waves on Wind-Wave Growth with Fetch: An Experimental Study

ANTOINE VILLEFER,[a,b,c] MICHEL BENOIT,[a,c] DAMIEN VIOLEAU,[a,b] CHRISTOPHER LUNEAU,[d] AND HUBERT BRANGER[c]

[a] *EDF R&D/LNHE, Chatou, France*
[b] *Laboratory for Hydraulics Saint-Venant, Chatou, France*
[c] *Aix Marseille Univ, CNRS, Centrale Marseille, Institut de Recherche sur les Phénomènes Hors-Equilibre (UMR 7342), Marseille, France*
[d] *Institut Pythéas, Aix Marseille Univ, CNRS, IRD, Marseille, France*

(Manuscript received 4 March 2021, in final form 19 August 2021)

ABSTRACT: A series of experiments were conducted in a wind-wave tank facility in Marseilles (France) to study the effects of preexisting swell conditions (represented by long mechanically generated waves) on wind-wave growth with fetch. Both monochromatic and irregular (JONSWAP-type) long-wave conditions with different values of wave steepness have been generated in the presence of a constant wind forcing, for several wind velocities. A spectral analysis of temporal wave signals combined with airflow measurements allowed for the study of the evolution of both wave systems with the aim of identifying the interaction mechanisms transportable to prototype scale. In particular, a specific method is used to separate the two wave systems in the measured bimodal spectra. In fetch-limited conditions, pure wind-wave growth is in accordance with anterior experiments, but differs from the prototype scale in terms of energy and frequency variations with fetch. Monochromatic long waves are shown to reduce the energy of the wind-waves significantly, as it was observed in anterior laboratory experiments. The addition of JONSWAP-type long waves instead results in a downshift of the wind-wave peak frequency but no significant energy reduction. Overall, it is observed that the presence of long waves affects the wind-wave energy and frequency variations with fetch. Finally, in the presence of JONSWAP-type long waves, variations of wind-wave energy and peak frequency with fetch appear in close agreement with the wind-wave growth observed at prototype scale both in terms of variations and nondimensional magnitude.

KEYWORDS: Ocean; Wave properties; Wind stress; Wind waves; Sea state; Air-sea interaction; Laboratory/physical models

## 1. Introduction

The infinite diversity of waves in the ocean makes the understanding of the complex sea states dynamics rather difficult. Numerous experimental studies both in the field and in laboratories have been carried out over the last decades to improve the knowledge on the particular case of bimodal sea states or, more precisely, on wind-wave and swell combination. Many field measurements (Donelan et al. 1997; Hwang et al. 2011; Vincent et al. 2019) show evidence of a modified wind-wave generation in the presence of swell. However, field experiments can hardly be generalized due to the specific wind and atmospheric conditions varying from one experiment to another. In wind-wave tank facilities, wind-wave and swell combination can be studied in controlled conditions using a wave-maker (e.g., a mechanically actuated paddle) for representing swell and a closed-loop air circulation to produce a quality airflow creating short wind waves above the long mechanically generated waves (paddle waves). Thereby, both wave systems are sufficiently separated in frequency to observe a bimodal sea state. A series of experiments was conducted in a well-controlled laboratory environment in Marseilles (France) with two objectives. The first one was to identify the mechanisms at stake in the interaction between the two wave systems. Assessing the extent at which those mechanisms can be transposed to wind-wave growth in the ocean was the second objective.

The wind-wave generation over a train of long monochromatic paddle waves propagating along the wind direction is a well-documented experimental configuration (Mitsuyasu 1966; Phillips and Banner 1974; Donelan 1987). In these conditions, a drastic reduction on the energy density of the wind-wave component is unanimously observed. The intensity of this reduction increases with the long-wave steepness $ak$ (where $a$ is the wave amplitude and $k$ the wavenumber). Donelan (1987) found a wind-sea elevation variance reduced by a factor of about 2.5 in presence of long waves. A similar experiment by Mitsuyasu and Yoshida (1991) with long waves propagating opposite to the wind direction revealed wind-wave height intensification. More recently, Benetazzo et al. (2019) and Bailey et al. (2020) carried out experiments (in an open-air basin without a closed-loop airflow in the case of Bailey et al.) on wind over irregular [Joint North Sea Wave Project (JONSWAP)-type] paddle waves. These latter experiments also showed a reduced wind-wave growth.

Variance density spectrum $E(f, \theta, x, t)$ at a location $x$ and a time $t$, where $f$ and $\theta$ are the wave frequency and direction,

*Corresponding author*: Antoine Villefer, antoine.villefer@edf.fr

DOI: 10.1175/JPO-D-21-0050.1

respectively, is a powerful manner to describe wind-wave growth. For infinite depth, the evolution of $E(f, \theta, x, t)$ is governed by the spectral energy balance involving source/sink terms $S(f, \theta, x, t)$:

$$\frac{dE}{dt} = S_{\text{in}} + S_{\text{ds}} + S_{\text{nl}}. \tag{1}$$

The left-hand side is the kinematic part of the equation while the right-hand side includes three source/sink terms corresponding to wind energy input $S_{\text{in}}$, dissipation through whitecapping $S_{\text{ds}}$, and nonlinear four-wave interactions $S_{\text{nl}}$. Note that among these terms, only the latter one is explicitly formulated based on a weakly nonlinear theory (Hasselmann 1962) while the formulations used for $S_{\text{in}}$ and $S_{\text{ds}}$ rely on semiempirical parameterizations of complex sea–atmosphere interaction processes [see Cavaleri et al. (2007) for a review and discussion of these terms].

Experiments of wind over monochromatic mechanically generated waves propagating in the same direction have received a lot of attention to provide a physical explanation to wind-wave reduction and to consider at what extent this effect could appear at natural scale. First, the hypothesis of an enhanced wave breaking of the wind sea, represented by $S_{\text{ds}}$, due to the addition of wind drift and long-wave orbital velocities, was suggested by Phillips and Banner (1974). This suggestion was later shaded by Wright (1976), arguing that enhanced wave breaking could not account for the magnitude of wind-wave reduction in the case of high wind velocities. According to Masson (1993), nonlinear four-wave interactions (i.e., $S_{\text{nl}}$) are also involved in the physical evolution when the ratio of long-wave to short-wave frequency is greater than 0.6. This ratio discriminates the interaction between wind waves and swell in the ocean (ratio lower than 0.6) and in most laboratory experiments (ratio greater than 0.6).

Chen and Belcher (2000) developed a model based on a sheltering effect of the long waves absorbing momentum from the wind, thus reducing the available momentum for wind-wave generation (i.e., $S_{\text{in}}$). Their model delivered results in accordance with laboratory experiments but closely depending on the growth rate coefficient $\beta$ formulated by Miles (1957) as $S_{\text{in}} = \beta E$, which is known to be highly variable, especially at laboratory scale. The growth rate coefficient itself depends on the long-wave age $C/u_\star$, with $C$ the long-wave (phase) celerity, and $u_\star = (\tau/\rho)^{1/2}$ the friction velocity with $\tau$ the total turbulent shear stress at the air–water interface, and $\rho$ the air density. Chen and Belcher's results suggest that the wind-wave reduction observed in laboratory environment with young waves ($C/u_\star \ll 20$) would probably not occur with older ocean swell for which $C/u_\star > 20$. More directly, Chen and Belcher's model predicts that the sheltering effect occurs when the long waves are, to a good extent, slower than the wind. Lately, Donelan et al. (2010) attributed the wind-wave reduction to both the modified airflow (i.e., $S_{\text{in}}$) and the orbital velocity gradients in the presence of the long waves.

In our experiment, short waves were generated by the wind in a large closed-loop wind/wave tank facility, and long waves were generated with a wave-maker, with both cases of monochromatic waves and irregular (JONSWAP-type) waves. All the measurements were carried out on a fetch-limited wave field. The fetch limited case is a generic case of spatial wave evolution consisting in a steady wind forcing over a statistically stationary wave field. The statistical wave field can be related to the wave-spectrum notion.

To compare our experimental results with other laboratory experiments and field observations, an appropriate scaling has to be applied. Following Kitaigorodskii (1961), the parameters describing wind-wave growth are the total variance of the free-surface elevation $m_0 = \overline{\eta^2}$ and the peak frequency $f_p$ as a function of the fetch $X$. Those variables are made dimensionless using the friction velocity $u_\star$ and the acceleration due to gravity $g$:

$$f_p^* = \frac{f_p u_\star}{g}, \tag{2}$$

$$m_0^* = \frac{m_0 g^2}{u_\star^4}, \tag{3}$$

$$X^* = \frac{Xg}{u_\star^2}. \tag{4}$$

Although the wind speed at 10 m above the mean free surface $U_{10} = U(z = 10\,\text{m})$ is usually employed as a scaling wind speed, the friction velocity is chosen here since it does not depend on height and it better represents the momentum transfer at the air/water interface (Janssen 2004).

The facility and the data processing methods are introduced in section 2. The wind profiles determined in presence and in absence of paddle waves, used as a scaling tool for the subsequent analyses, are presented in section 3. The growth of wind waves is measured and processed in absence of long waves in section 4, then in presence of monochromatic waves in section 5 and finally with irregular waves in section 6. A comparison of these different cases and their relation with the prototype scale are discussed in section 7. Section 8 gives a summary of results and their application, followed by a further discussion on future studies on the topic.

## 2. Experimental facility and data processing

### a. The facility

The Institut de Recherche sur les Phénomènes Hors-Equilibre (IRPHE)–Pythéas wind-wave tank (see Fig. 1) consists of a closed-loop tunnel for air circulation with a 1.5-m-high air cavity above a basin with a test section 40 m long and 2.60 m wide (sketched in Fig. 2). The water depth $h$, set to 0.80 m, was kept constant during all the experiments. For a complete description of the facility, one can refer to Coantic et al. (1981). The wind is generated by an air blower in the upper part of the tunnel and guided through a settling chamber with a honeycomb and a converging nozzle; this system produces a uniform airflow at the entrance of the water basin. At the upwind end of the basin, an immersed paddle wave-maker (piston-type) can be used for generating either monochromatic or irregular waves propagating along the wind direction. At the downwind end, a permeable absorbing beach with a 6° slope was installed to minimize wave reflection. The basin sidewalls

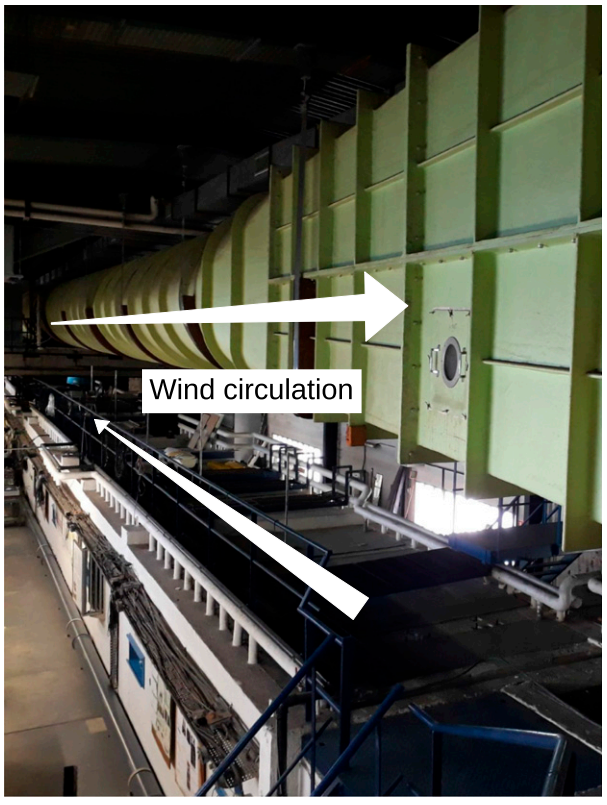


FIG. 1. Upwind view of the IRPHE–Pythéas wind-wave tank in Marseilles. The top and left sides of the closed water + air tunnel can be seen in the lower part of the picture, while the green pipe in the upper part is part of the recirculating air tunnel (see text for additional description).

are punctuated with windows to observe the water surface. A larger 5-m-long clear glass is situated at the 25-m fetch to perform measurements that require a sight on the water surface.

For these experiments, eight resistance-type and four capacitance-type wave gauges were distributed along the basin (Fig. 3) to measure the instantaneous free surface elevation $\eta$ with a precision of $4 \times 10^{-4}$ and $2 \times 10^{-4}$ m, respectively. Note that the wave gauges distribution is not uniform: the distance between two consecutive gauges decreases at large fetch (Fig. 2). Two anemometers were situated in front of the clear glass at a 25-m fetch (Figs. 2 and 3). Wind reference velocity $U_{\text{ref}}$ was measured at approximately 0.5 m above the water surface with a Gill 2D sonic anemometer.

An additional hot film anemometer from E+E Electronik supported by a vertical telescopic pole allowed to measure the vertical profile of the mean (i.e., time averaged) horizontal velocity $U(z)$. Friction velocity and aerodynamic roughness $z_0$ are determined by fitting the logarithmic profile (see section 3) to the vertical time-averaged wind profile in neutral atmospheric conditions for all the experiments (air and water were roughly at the same temperature). The friction velocity is considered constant along the test section because of the slightly divergence of the air section along the wind-wave tank allowing a zero pressure longitudinal gradient.

Apart from the air blower controlled with a graduated potentiometer, the control of the wave-maker and all the gauges output signals were gathered on a computer using a LabView program. Wind velocity could be generated between 2 and 14 m s$^{-1}$ ($U_{\text{ref}}$) by regulating the potentiometer.

To generate waves, the required temporal free surface elevation was convoluted with the wave-maker transfer function, and then transferred as a voltage signal from the computer to the piston wave-maker, converting the input signal to actual waves. Both regular (Stokes-type) and irregular (JONSWAP-type) wave trains were generated. The JONSWAP spectrum is given by

$$E(f) = \alpha_p H_s^2 \frac{f_p^4}{f^5} \exp\left[-\frac{5}{4}\left(\frac{f_p}{f}\right)^4\right] \gamma^{\exp\left[-\frac{(f-f_p)^2}{2\sigma^2 f_p^2}\right]}, \quad (5)$$

where, using the JONSWAP's recommendations (Hasselmann et al. 1973), $\sigma = 0.07$ for $f < f_p$ and $\sigma = 0.09$ for $f > f_p$, $\gamma = 3.3$ is the peak enhancement factor and $\alpha_p = 0.2$ is the Phillips constant. The significant wave height $H_s$ and the peak frequency $f_p$ are the parameters to adjust in order to obtain the desired sea state.

To generate the time series of irregular waves, inverse FFT (fast Fourier transform) transforms of the complex amplitudes from the JONSWAP spectra (using random phases) were used over the frequency range 0.4–4.0 Hz. This wide range of frequency, which is the recommended mechanical range for the wave-maker, was necessary in order to obtain a smooth transition between the JONSWAP peak and the high-frequency waves. However, the wave-maker was able to accurately generate a sea state corresponding to a JONSWAP-type spectrum over the frequency range 0.4–2.0 Hz. Above 2 Hz the energy distribution could slightly deviate from the $f^{-5}$ desired tail.

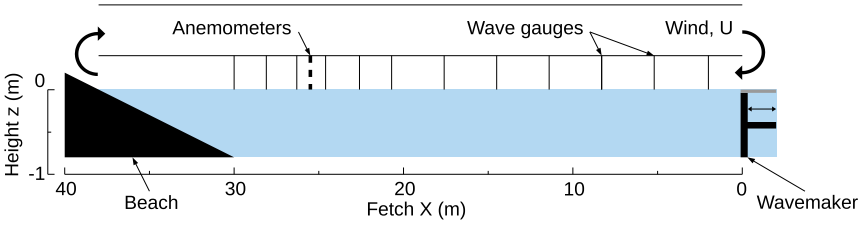


FIG. 2. Sketch of the IRPHE–Pythéas wind-wave tank facility showing the location of the measuring devices. The vertical exaggeration is ×5.

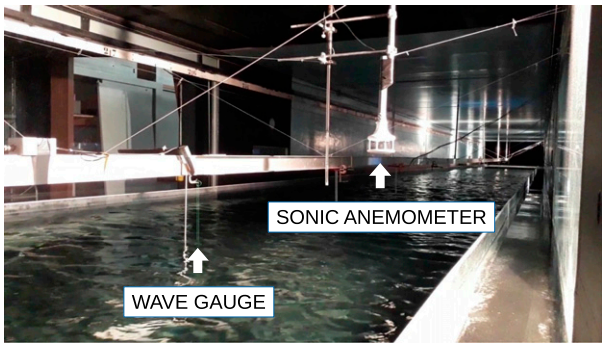


FIG. 3. Downwind view of the inside of the wind-wave tank with a generic case of long monochromatic paddle waves and short wind waves.

Acquisition of wave gauges signals were launched from the computer for a 20-min duration at the sampling rate of 256 Hz. Before every acquisition, it was verified that the waves in the wave tank were in stationary fetch-limited conditions by waiting a sufficient long time before acquiring data. During the experiments with wind, the instantaneous horizontal wind velocity was measured using the hot film anemometer from the lower point above the water surface (i.e., slightly above the highest wave) at about ten vertically distributed points over a range of 20 cm and a duration of 240 s to obtain the vertical profile of the mean horizontal velocity. To be able to differentiate swell from wind waves, the mechanically generated wave frequency (respectively the peak frequency for irregular waves) was chosen equal to 0.6 Hz. This choice accounts for the wind waves' lower peak frequency reaching 1 Hz at maximum fetch and maximum wind velocity.

Using the dispersion relation for the long waves, the nondimensional depth $kh = 1.33$ corresponds to intermediate water depth. Thus, bottom friction slightly dissipates the paddle waves as they propagate along the tank. Bottom friction and additional dissipation mechanisms, such as sidewalls friction, that occur in laboratory experiments have been quantified using Dorn's formula (Dorn 1966). At the downwind end of the tank, more than 95% of the long wave energy is conserved. Wind waves, however, are short enough ($kh > 3$) to be considered as propagating in deep water and unaffected by bottom friction. Wind-wave dissipation by sidewalls remains weak since their wavelengths is much smaller than the channel width (Shemer 2019). Overall, the dissipation due to bottom and sidewalls friction is relatively low and is not further considered in the present study.

Table 1 gathers the characteristics of all the tests presented in this paper.

### b. Spectral separation methods

A spectral approach was chosen to characterize the interaction between wave systems. Spectra were calculated using the Welch method (Welch 1967) by partitioning the surface elevation time records into shorter records of 16 384 points with a 50% overlap and a Hanning windowing. Depending on the sea states, the resulting spectra were unimodal (wind waves only, irregular swell only) or multimodal (monochromatic swell with harmonics, swell, and wind waves combination). Separating wave systems in multimodal sea states is necessary to have access to their individual characteristics (e.g., significant wave height, peak period, spectral width) in order to compare wind-sea growth with and without swell for instance. In the literature, this separation is commonly performed using a transition frequency that divides the wave spectrum in two parts: swell and wind sea. That method works while the peaks of both wave systems are sufficiently separated. In some cases, as it will be shown in this paper, wind-sea and swell components are overlapping, making difficult the separation with the former method. Two methods to separate the mechanically generated wave part from the wind-wave part of

TABLE 1. Wind characteristics and corresponding power law coefficients representing the fetch dependence of wind-sea peak frequency and energy [$m_0^* = b(X^*)^c$ and $f_p^* = d(X^*)^g$]. The lines with bold characters refer to the pure wind-sea cases.

| | | | | |
|---|---|---|---|---|
| $U_{ref}$ (m s$^{-1}$) | | 6 | 10 | 14 |
| $U_{10}$ (m s$^{-1}$) | | 9 | 13 | 20 |
| $u_*$ (m s$^{-1}$) | | 0.31 | 0.48 | 0.88 |
| $z_0 \times 10^4$ (m) | | 1.4 | 1.6 | 9.3 |
| Swell type | $ak$ (%) | | ($b \times 10^4$, $c$) | |
| Monochromatic | 5.6 | (0.13, 1.28) | (0.59, 1.05) | — |
| | 2.7 | (2.00, 0.99) | (0.31, 1.29) | (4.61, 0.82) |
| | **0.0** | **(0.02, 1.64)** | **(0.11, 1.50)** | **(0.52, 1.30)** |
| Irregular | 2.7 | (2.16, 1.01) | (0.96, 1.17) | (1.27, 1.18) |
| | 4.1 | (2.68, 1.01) | (7.56, 0.90) | (5.47, 0.91) |
| Swell type | $ak$ (%) | | ($d$, $g$) | |
| Monochromatic | 5.6 | (0.60, −0.28) | (0.64, −0.30) | — |
| | 2.7 | (1.68, −0.42) | (1.27, −0.38) | (0.86, −0.33) |
| | **0.0** | **(3.46, −0.50)** | **(1.36, −0.39)** | **(0.89, −0.33)** |
| Irregular | 2.7 | (0.06, −0.01) | (0.28, −0.20) | (0.34, −0.22) |
| | 4.1 | (0.11, −0.11) | (0.07, −0.02) | (0.21, −0.14) |

multimodal spectra are introduced in this section. The first method deals with the multimodal sea states with a monochromatic swell. The second method refers to multimodal sea states with a JONSWAP-type swell. Both methods are based on curve-fitting using a nonlinear least squares method, and are described below.

The generation of monochromatic long waves with the wave-maker leads to the generation of additional superharmonic waves in intermediate depth conditions. These harmonics occupy the same frequency range as the wind sea making difficult the distinction between the proper energies and peak frequencies of these overlapping systems. The first stage of the method consists in the removal of the spectral bands containing the frequencies of the monochromatic wave harmonics into the initially measured multimodal spectrum. The removed number of points depends upon the width of the corresponding harmonic peaks. Thus, although the wind-wave peak then becomes discontinuous at this stage, its shape is conserved. The next stage is to fit the discontinuous wind-wave spectral peak with a JONSWAP-type spectrum initialized with the triplet ($f_p$, $H_s$, $\gamma = 3.3$). The significant wave height $H_s$ is equal to the integral of the spectrum and the peak frequency $f_p$ is equal to the maximum value of the spectrum. The fitted JONSWAP-type spectrum enables to access the energy and the peak frequency of the wind-wave part of the spectrum. Then, the harmonic-only part of the spectrum can be obtained by subtracting the fitted wind-wave part from the measured multimodal spectrum.

A spectrum combining irregular-swell and wind waves can be decomposed using the following procedure inspired from Mackay (2011). First, a unimodal JONSWAP-type spectrum $E^+$ [see (5)] is fitted on the bimodal measured spectrum $E_m$ using the triplet ($f_p^+$, $H_s^+$, $\gamma^+ = 3.3$) as initial values: $H_s^+$ is determined using the integral of $E_m$ and $f_p^+$ is equal to the frequency of the higher peak. For this first fit, the peak frequency is a constant parameter in order to fit the higher peak only. The resulting fitted triplet is ($f_p^+$, $H_s^{+\prime}$, $\gamma^{+\prime}$) (the prime denoting the fitted parameters). A second triplet ($f_p^-$, $H_s^-$, $\gamma^- = 3.3$) is used as initial value to fit the second (i.e., the lower) peak with $H_s^-$ from the integral of $E^- = E_m - E^+$ and $f_p^-$ as the peak frequency of $E^-$. Finally, the sum of two JONSWAP-type spectra (i.e., bimodal) $E^- + E^+$ is fitted on the bimodal measured spectrum $E_m$ using both ($f_p^-$, $H_s^-$, $\gamma^-$) and ($f_p^+$, $H_s^{+\prime}$, $\gamma^{+\prime}$) as initial values of the least squares algorithm. Thus, the measured spectrum is decomposed in two JONSWAP-type spectra permitting to determine the energy and peak frequency of each wave system.

An illustration of the spectral separation of a measured bimodal spectrum is given in Fig. 4. The figure shows that the spectra resulting from the spectral separation are an accurate fit for both long-wave and wind-wave peaks but slightly deviate from the measured spectrum in the high-frequency range. It is also interesting to note the slight reduction of wind-wave energy at the peak of the wind-wave spectrum whether the spectrum is separated or included in the bimodal spectrum. This last observation proves the necessity of a proper separation of each wave system in a multimodal measured spectrum so that they can be compared to the wave systems observed individually in unimodal measured spectra as it will be performed in the following.

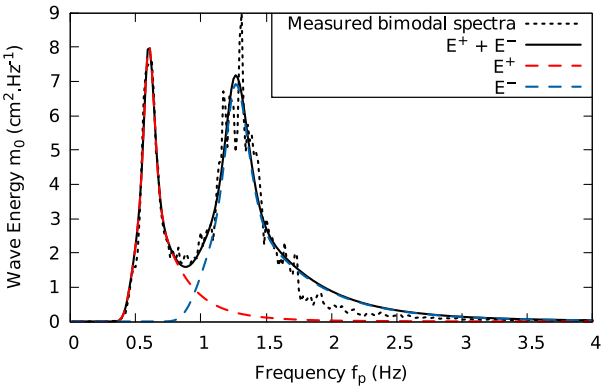


FIG. 4. Example of spectral separation for a spectrum obtained at a 30-m fetch with a wind of 10 m s$^{-1}$ in presence of irregular long waves of 2.7% steepness; $E^+$ and $E^-$ are respectively the JONSWAP fit of the higher and the lower peaks.

## 3. Estimation of the vertical wind profile

Among the numerous methods for estimating wind fluxes, the profile method was used for this experiment. Thus, the airflow above water waves is considered analogous to that above a stationary rough surface. Assuming a constant flux layer and using the Monin and Obukhov (1954) turbulence similarity theory, the vertical velocity wind profile is assumed logarithmic and may be written as

$$U(z) = \frac{u_\star}{\kappa} \ln\left(\frac{z}{z_0}\right), \tag{6}$$

where $\kappa = 0.41$ is the von Kármán constant, $z$ is the coordinate on a vertical axis pointing upward with origin at the mean water level (MWL) (see Fig. 2) and $z_0$ is the aerodynamic roughness. The measured vertical evolution of the mean horizontal wind velocity is fitted with the logarithmic turbulent velocity profile (6). In that way, the friction velocity and the aerodynamic roughness are found for cases with and without paddle waves.

Figure 5 displays the vertical profiles of the averaged horizontal wind velocity with and without paddle waves, for monochromatic and irregular waves. The measured wind velocities have an overall tendency to increase when paddle waves are present. Regarding the fitted logarithmic profiles, paddle waves have a trend to increase the friction velocity, thus inducing an increase in the total shear stress $\tau$ at the air/water interface. This observation is not surprising since the wind stress is mainly supported by waves traveling slower than the wind, which is the case for both wind waves and paddle waves in our experiments. Those results are in disagreement with Chen and Belcher (2000) who designed a model for the reduction of wind waves due to long monochromatic waves based on the absence of variation of the total stress with long-wave steepness.

However, the large error bars corresponding to the standard deviation in the calculation of the mean horizontal velocity

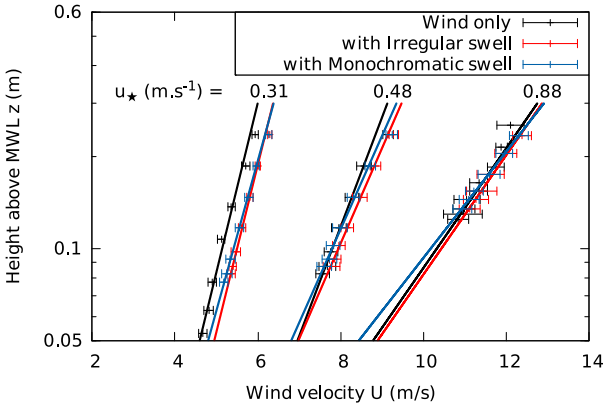


FIG. 5. Vertical profiles of the averaged horizontal wind velocity with and without paddle waves associated logarithmic fits. The corresponding friction velocities values (mean slope of the fitted lines) are indicated for each wind-only case.

depicted in Fig. 5 show the uncertainties associated with the logarithmic fit. Thus, there is a high degree of uncertainty in the estimation of $u_\star$. Regarding the measurements, two evaluations of the friction velocity in the same experimental conditions could lead to a 20% variation in the results. Additionally, water sprays at high wind speed (e.g., $U_{\text{ref}} = 14\,\text{m}\,\text{s}^{-1}$) could invalidate the measurements by reaching the hot film and cooling down its temperature, thus measuring abnormally high velocities. Overall, the use of the logarithmic profile method to determine the friction velocity and the aerodynamic roughness seems questionable since the presence of long waves propagating slower than the wind is prone to invalidate the analogy with the airflow above a stationary rough plate. A method free from the logarithmic profile hypothesis, such as the eddy-correlation method using a thin cross-X hot wire anemometer, would be more adapted for the characterization of the airflow in the presence of paddle waves; this is left for further work.

Due to the uncertainties previously mentioned, the measured data will be scaled using a unique friction velocity for each wind speed. This friction velocity is determined using the profile method on pure wind-sea cases (see Fig. 5). Thus, the measurement uncertainties added by the presence of long waves are avoided, and possible effects of such waves on the wind friction velocity will be ignored. Shemer (2019) observed that the friction velocity does not depend notably on the fetch in a similar fetch-limited case. Using this latter observation in our study, the friction velocity is assumed to be constant along the fetch with an impact of the surface drift velocity considered as negligible (Shemer 2019).

## 4. Wind-wave growth

This section aims to verify the similarities on fetch-limited wind-wave growth between our results, anterior laboratory experiments and ocean measurements. In this section, experimental data with wind only (i.e., without mechanically generated waves) are analyzed.

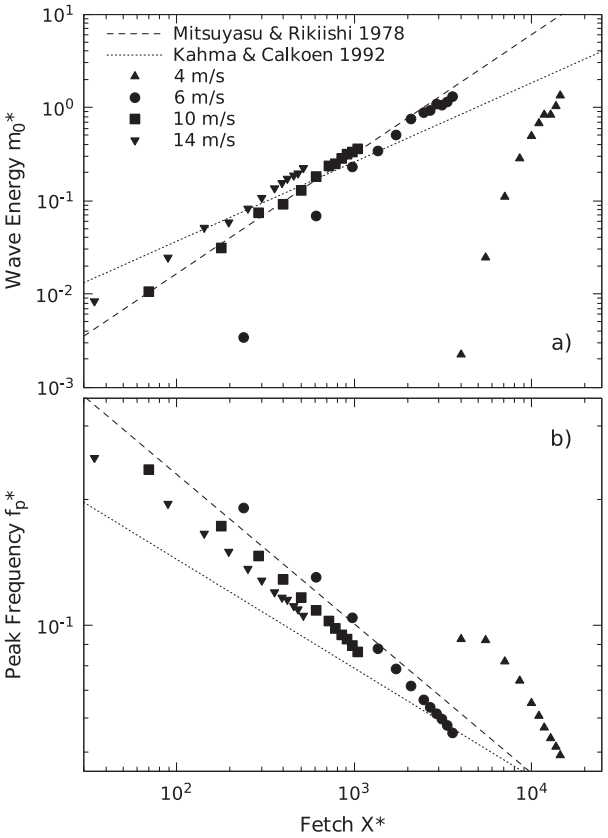


FIG. 6. Variations of (a) dimensionless wave energy and (b) peak frequency with dimensionless fetch for different reference wind speeds ($U_{\text{ref}}$) compared to empirical laws.

Laboratory experiments are, on one hand, necessary to facilitate the understanding of wind-wave growth through controlled conditions. On the other hand, limitations are present due the limited size and the peculiarities from a wave tank to another. To quantify these limitations, fetch-limited cases of wind-wave growth under four increasing wind velocities have been carried out in the wind-wave tank. In Fig. 6, the evolution of the measured dimensionless wind-wave energy and peak frequency are plotted and compared to two selected empirical laws. The first one is Mitsuyasu and Rikiishi's (1978) law exclusively based on laboratory experiments:

$$m_0^* = 4.49 \times 10^{-5}(X^*)^{1.282} \quad \text{and} \quad f_p^* = 1.19(X^*)^{-0.357}. \tag{7}$$

The second one is Kahma and Calkoen's (1992) law for stable stratification (adapted to friction velocity scaling from Komen et al. 1994) obtained from a collection of laboratory and ocean data:

$$m_0^* = 7.3 \times 10^{-4}(X^*)^{0.85} \quad \text{and} \quad f_p^* = 0.477(X^*)^{-0.26}. \tag{8}$$

Figure 6 shows the differences in wind-wave growth depending on the wind speed in our experiments. At high wind speed, $U_{\text{ref}} \geq 10\,\text{m}\,\text{s}^{-1}$, energy and peak frequency exhibit a linear evolution with fetch in log–log coordinates confirming a power law behavior. Additionally, this power

law appears to be in accordance with Mitsuyasu and Rikiishi's (1978) law.

At lower wind speed, water surface tension affects the evolution of wind-wave energy (Fig. 6a), especially because most of the waves are short, hence in the capillary-gravity range, where surface tension strongly modifies the wave dynamics. The case $U_{ref} = 6\,m\,s^{-1}$ is characterized by a two-stage evolution that clearly appears in the energy variation: the first stage, $X^* < 10^3$, shows a strong slope which is attenuated, in a second stage, at larger fetches. Surface tension impact thus decreases gradually as the waves grow. The second stage, $X^* > 10^3$, is linear and parallel to Mitsuyasu and Rikiishi's power law indicating that the surface tension effect on waves is lower. Wind waves generated by a $4\,m\,s^{-1}$ wind deviate markedly from both the experimental curves for higher wind speeds and empirical laws: surface tension seems to have a significant effect in that case.

Moreover, both dimensionless energy and peak frequency magnitudes agree reasonably well with Kahma and Calkoen's law. The differences with this latter law lie in the variations of the variables with fetch. Since Mitsuyasu and Rikiishi's law is a good fit for our experimental data variations, absolute value of the power coefficients from Kahma and Calkoen's law [0.85 for the energy, 0.26 for the peak frequency in (8)] appear somewhat too low to accurately describe laboratory data [corresponding exponents are 1.282 for the energy, 0.357 for the peak frequency in (7)]. Recently, Shemer (2019) also fitted power laws to a set of small-scale experiments, and found exponents in rather good agreement with the values obtained here, namely, 1.012 for the energy and 0.27 for the peak frequency.

Another relevant comparison with empirical law can be done using Toba's 3/2 law (Toba 1997):

$$H_s^* = 0.062(f_p^*)^{3/2} \tag{9}$$

or in term of energy formulation

$$m_0^* = 2.4 \times 10^{-4}(f_p^*)^3. \tag{10}$$

This law is well adapted to ocean measurements. Contrary to power law previously mentioned the fetch does not appear in this relation. This is a benefit since the fetch is difficult to define in the real ocean because of the wind changing speed and direction. Note that the previous two sets of laws (7) and (8) disagree with Eq. (10) in the sense that the ratio of their power coefficients is slightly above the value of 3 as claimed by Toba.

Figure 7 shows the agreement between our experimental results and Toba's law. In line with Fig. 6, Fig. 7 shows that once wind waves are long enough to be free from surface tension effect (i.e., below a certain peak frequency or above a certain wind speed) Toba's law is well adapted to describe our experimental dataset.

This section proved that laboratory experiments are, to a good extent, appropriate to describe short fetch evolution of a growing wind sea in the ocean. From this observation, long mechanically generated waves representing swell are now added to the system in order to observe their effect on the growing wind sea.

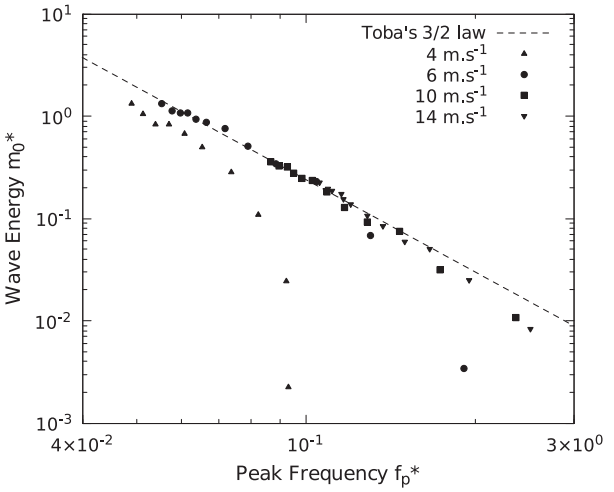


FIG. 7. Variations of the wind-wave dimensionless energy with the dimensionless peak frequency for different equivalent wind speed ($U_{ref}$) compared to variations according to Toba's 3/2 law (10).

## 5. Effect of monochromatic paddle waves on wind-wave growth

To assess the effect of (following) swell on wind-wave growth we repeated the same wind forcing conditions of the previous section with now long monochromatic paddle waves generated at $X = 0\,m$ with the wave-maker. Two values of steepness of these long waves were considered: $ak = 2.7\%$ and $ak = 5.6\%$, with $a = H/2 = \sqrt{2m_0}$ the wave amplitude, corresponding to wave frequency $f = 0.6\,Hz$. In both cases, the long waves have a moderate level of nonlinearity, lying in the validity domain of Stokes' second-order wave theory. As will be seen hereafter, harmonic modes of the fundamental forcing frequency will be present in the analyzed spectra.

In the wave tank, the addition of these regular long waves had the direct and visible effect of attenuating the wind waves. Figure 8 illustrates this interaction through the spatial evolution of the variance density spectrum for the wind speed $U_{ref} = 10\,m\,s^{-1}$. For that purpose, the pure wind-wave spectrum is compared to the spectrum combining wind waves and paddle waves.

The semilog scale in Fig. 8 emphasizes the generation of wind waves at high frequencies. At short fetch (from 0 to 10 m), wind-wave peak frequency in the presence of long waves deviates from the pure wind-wave peak frequency: the wind-wave peak frequency becomes lower as the steepness of the long-wave increases. This downshift is even more pronounced at a lower wind speed (not shown here). The frequency deviation from the pure wind-sea growth is also depicted in Fig. 9b using the spectral decomposition presented in section 2b. A possible explanation for this downshift is the presence of high-frequency harmonics initiating wind-wave growth at frequencies lower than in the absence of paddle waves. The induced frequency shift reduces at larger fetch and eventually vanishes. Thus, the progression of the wind-wave peak toward low frequencies is slowed down in the presence of long monochromatic waves.

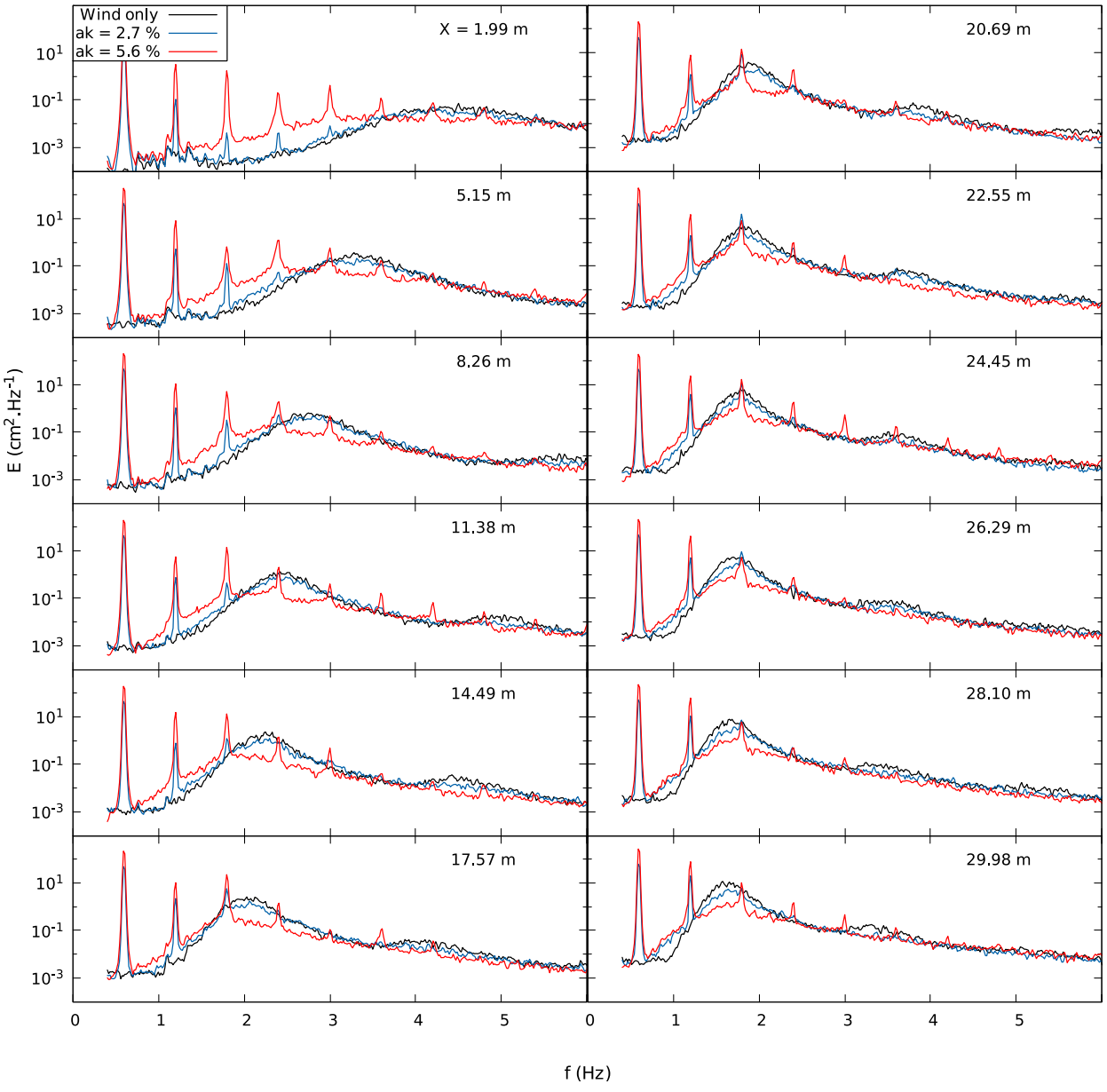


FIG. 8. The spatial evolution of the variance density spectrum with and without regular paddle waves of steepness $ak$ and peak frequency 0.6 Hz for a wind speed $U_{\mathrm{ref}} = 10\,\mathrm{m\,s^{-1}}$.

Donelan (1987) drew attention to the slowed rate of progression of the paddle-modified wind-sea peak toward low frequencies with increasing fetch. In his 100-m-long tank, the introduction of long waves upshifted the wind-sea peak frequency at large fetch ($X \sim 70\,\mathrm{m}$). This tendency of the pure wind-sea peak to overtake the paddle-modified one in its progression toward low frequencies could be imagined as a scenario in our case with an extended fetch: in Fig. 9b, a hypothetical spatial extension of the $ak = 5.6\%$ peak frequency evolution toward higher fetch would probably lead to the observation of Donelan. According to him, the frequency shift previously described could be due to an alteration of the dispersion relation when a paddle wave passes through a group of wind waves, resulting in a detuning of the resonance leading to a modified nonlinear quartet interaction. This hypothesis is also relevant to explain the broadening of the paddle-modified wind-wave peak in its forward face (low frequency).

Regarding the relative energy of wind waves, paddle waves broaden and flatten the corresponding spectral peak (Fig. 8) resulting in a total energy ($m_0$, see Fig. 9a) smaller than the total energy of pure wind sea. This observation is in line with previous studies (Mitsuyasu 1966; Phillips and Banner 1974; Donelan 1987).

In Fig. 9, the evolution of wind-wave energy and peak-frequency with fetch using log-scaled axes can be approximated

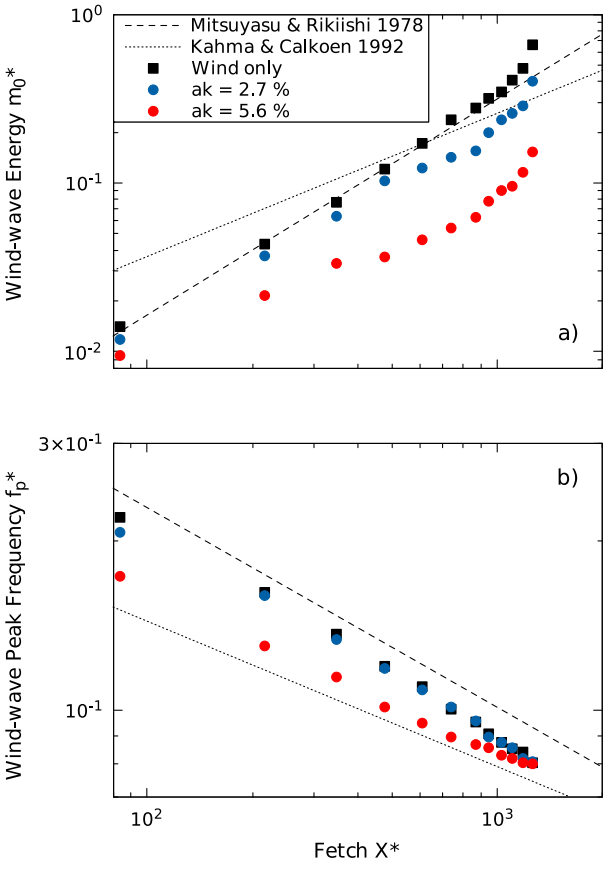


FIG. 9. The spatial evolution of (a) wind-wave energy and (b) peak frequency with and without regular paddle waves of steepness $ak$ and peak frequency 0.6 Hz for a wind speed $U_{\mathrm{ref}} = 10\,\mathrm{m\,s^{-1}}$.

by straight lines. To extend the previous results for different wind speeds, the wind-wave growth curves observed in the tank are fitted with power laws in the same manner as the previously described empirical power laws. Table 1 gathers the power laws parameters providing a summary of our results on wind-wave growth with and without paddle waves for different wind speeds. In Table 1, the absolute values of coefficients $c$ and $g$ with monochromatic swell globally decrease with paddle waves' steepness, showing that both the variations of wind-wave energy and peak-frequency with fetch become milder.

The slowed increase of wind-wave energy with monochromatic paddle waves, that has been extensively studied in the past, has been related to wind-wave enhanced dissipation (Phillips and Banner 1974), long-wave sheltering effect (Chen and Belcher 2000) and nonlinear wave-wave interactions (Masson 1993). The sheltering effect can be observed in Fig. 8: at fixed wind speed and for a given fetch, wind-wave total energy decreases as the steepness of the paddle-wave increases. However, nonlinear wave–wave interactions are only significant when the ratio of long-wave to short-wave frequency is greater than 0.6 according to Masson (1993). This condition is not satisfied in our case considering the first harmonic of the monochromatic waves, with a ratio ranging from about 0.1 at $X = 1.99$ m to less than 0.4 at maximal fetch (Fig. 8). One can observe the second harmonic of paddle waves lies closer to the wind wave peak, but this peak corresponds to a bound wave component, so not fulfilling the linear dispersion relation and in principle not prone to resonant interaction with free wind-wave components.

In the high-frequency tail of the spectra in Fig. 8, a small wind-wave harmonic can be observed at about 2 times the wind-wave peak frequency, for the pure wind-wave case, and to a lesser extent with paddle waves of steepness $ak = 2.7\%$. It is hardly noticeable with paddle waves of steepness $ak = 5.6\%$. The decrease of this second harmonic peak as the long-wave steepness increases is a consequence of the reduction of the amplitude of the main wind-wave spectral peak with increasing long-wave steepness, resulting in a lower nonlinearity level of the wind wave component. Except for this difference, the high-frequency tail is not altered in the presence of paddle waves. This last observation is in disagreement with Donelan (1987) who noticed a higher tail for the cases including paddle waves.

A semilog scale is necessary to observe the high-frequency behavior of wave spectra but differences around the spectral peaks are usually less visible. Removing the semilog scale permits to discern the location of the significant energy in the spectra. Figure 10 shows the energy transfers differentiating so-called "pure" paddle waves (Fig. 10a) and "pure" wind waves (Fig. 10b) cases from the paddle-wave-plus-wind-wave combination (Fig. 10c) using a direct subtraction between the measured spectra. The pink area is a good illustration of the interaction between long monochromatic waves and short wind waves. The wind-wave reduction previously observed appears in the negative pink area between 1.25 and 2 Hz. The pink area under the first harmonic shows the amplification of the monochromatic paddle waves. A striking effect illustrated in Fig. 10 is the amplification of the second harmonic of the paddle waves by the wind: negligible in Fig. 10a, the second harmonic is prominent and even more amplified than the first harmonic in Fig. 10c. This amplification is a consequence of the frequency of the second harmonic of the fundamental mode of the paddle waves lying in the frequency band of the wind wave peak. Though less marked, this effect also manifests on the third harmonic at 1.8 Hz. In the same vein, it is observed in Fig. 8 that higher-order harmonics of the paddle waves are significantly amplified (see, for instance, the spectra with paddle waves of steepness $ak = 5.6\%$ for fetches from 10 to 20 m, for which the third harmonic is highly enhanced so has to become higher than the second harmonic. Thus, higher-order harmonics plays an important role in the interaction between both wave systems. These ideal waves enable a separation of the physical phenomena taking part into wave systems interactions. But adverse effects such as the amplification of wave harmonics can alter the direct comparison with ocean waves.

## 6. Effect of irregular paddle waves on wind-wave growth

To consider a more realistic long-wave system representing swell, a JONSWAP-type sea state was generated in the wave tank. The spatial evolution of the bimodal sea states with fetch is compared to the pure wind-sea case using a spectral

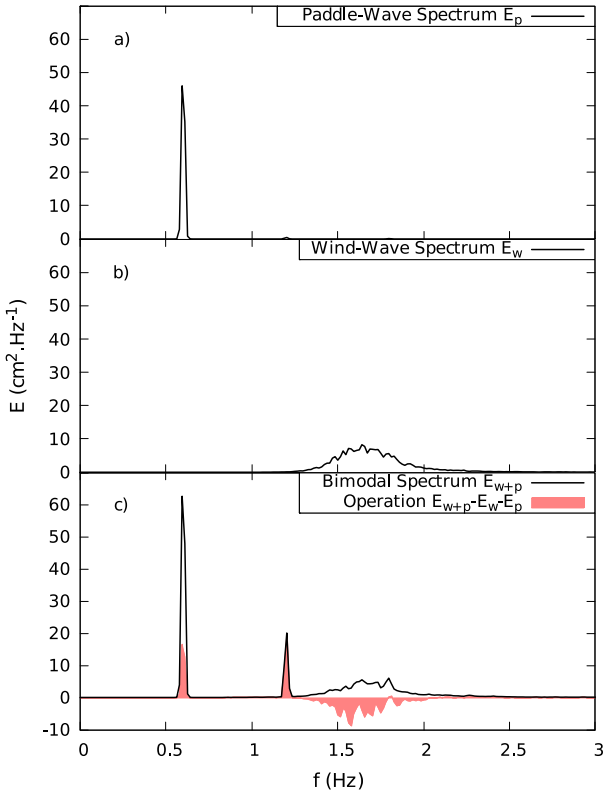


FIG. 10. (a) Pure paddle-wave spectrum $E_p$ and (b) pure wind-wave spectra $E_w$ by comparison with (c) the bimodal spectrum $E_{w+p}$ with monochromatic paddle waves of steepness $ak = 2.7\%$ and peak frequency 0.6 Hz at fetch of 30 m for a wind speed $U_{\text{ref}} = 10\,\text{m}\,\text{s}^{-1}$. The pink area is the difference between the bimodal spectrum $E_{w+p}$ and the sum of the pure spectra $E_w + E_p$.

representation in Fig. 11. In this section, the steepness $ak$ of the irregular waves is defined as $a = H_s/(2\sqrt{2}) = \sqrt{2m_0}$ and $k = k_p$. Using this definition, monochromatic and irregular waves with the same steepness have the same energy.

As in Fig. 8, the spatial evolution of spectra with fetch is shown in Fig. 11. A striking effect is the downshift of the wind-wave peak frequency in the presence of long irregular waves. This large downshift appears at the earliest stage of wind-wave growth (fetch $X = 1.99$ m in Fig. 11) and has the tendency to increase with increasing paddle-wave steepness. Thus, the presence of paddle-wave energy in the high-frequency range seems to initiate wind-wave growth with a lower frequency than without paddle waves. This effect, also observed in the monochromatic case, is even more pronounced with irregular long waves. The downshift then slightly reduces with fetch but remains significant even at the maximal fetch (i.e., $X = 29.98$ m). Figure 12b depicts different slopes in the nondimensional peak-frequency evolution depending on the presence of paddle waves and their relative steepness: the progression toward low frequency is slowed down with increasing paddle waves steepness.

Regarding the wind-wave energy, a small amplification effect due to long irregular waves is shown in Fig. 12a for the wind speed $U_{\text{ref}} = 14\,\text{m}\,\text{s}^{-1}$. This amplification, more significant at short fetch, has a tendency to reduce with increasing fetch. This reflects a slower energy variation with fetch in the presence of irregular paddle waves. At lower wind speed, this small amplification becomes a small reduction at the maximal fetch (see Table 1).

Overall, the effect of irregular waves on wind-wave energy appears weaker compared to monochromatic waves of the same energy. In the present study, the absence of a clear reduction of the wind-sea energy due to the presence of irregular paddle waves is in disagreement with Benetazzo et al. (2019) and Bailey et al. (2020). A plausible explanation for these diverging observations, based on Benetazzo et al. (2019), is an insufficient separation between the wave systems leading to a misinterpretation of the spectra combining wind waves and paddle waves. Using Fig. 11 to illustrate this latter remark, if one only considers the energy at the peak frequency of the pure wind sea, the presence of paddle waves indeed causes a wind-wave reduction at this particular frequency. Thus, it is only by considering the downshift that one can observe wind-wave energy has not been reduced but downshifted toward lower frequencies. Figure 10 in Benetazzo et al. (2019) shows that the wind-wave peak frequency downshift cannot be observed in their case due to the presence of the paddle-wave peak at 1 Hz. A lower paddle-wave frequency, in our case, permits the observation of this downshift.

The sheltering effect occurs especially with monochromatic paddle waves. The main characteristic differentiating these latter waves from the irregular waves is the distribution of wave energy over a range of frequencies. The wave trough between two consecutive crests of the dominant wave mode is much deeper with monochromatic paddle waves than with irregular ones. In the case of irregular paddle waves, the troughs are often "filled" with other wave modes causing lower height differences between crests and troughs than in the monochromatic case.

Regarding the slowed increase of wind-wave energy with fetch in the presence of irregular waves, since the sheltering effect is certainly reduced due to the spectral property, only enhanced dissipation and nonlinear wave–wave interaction are possible candidates. In this latter case, Masson's ratio is 0.6 at maximal fetch, implying a weak nonlinear interaction between wave systems. The remaining candidate would be the enhanced wave breaking due to wind-wave interaction with the addition of long-wave orbital velocities and wind drift as formulated by Phillips and Banner (1974).

The slowed rate of progression of the wind-sea peak toward lower frequencies with increasing fetch can be related to nonlinear interactions. With monochromatic paddle waves, Donelan (1987) suggested that the wind-wave energy transfer toward low frequencies might be reduced due to wind waves reduced steepness, thus nonlinearity, compared to pure wind sea. This latter suggestion can be illustrated in Fig. 13 where the wind-wave energy is expressed as a function of the wind-wave peak frequency. In this figure, the points representing wind-wave growth in the presence of paddle waves (blue and red dots for monochromatic and irregular paddle waves, respectively) are situated below the pure wind-wave growth (black dots). Thus, at a fixed wind-wave energy, the corresponding wind-wave peak frequencies in the presence of paddle waves are lower than in the pure wind sea case. Since a lower wave frequency relates to a lower wavenumber $k$ and the wave energy

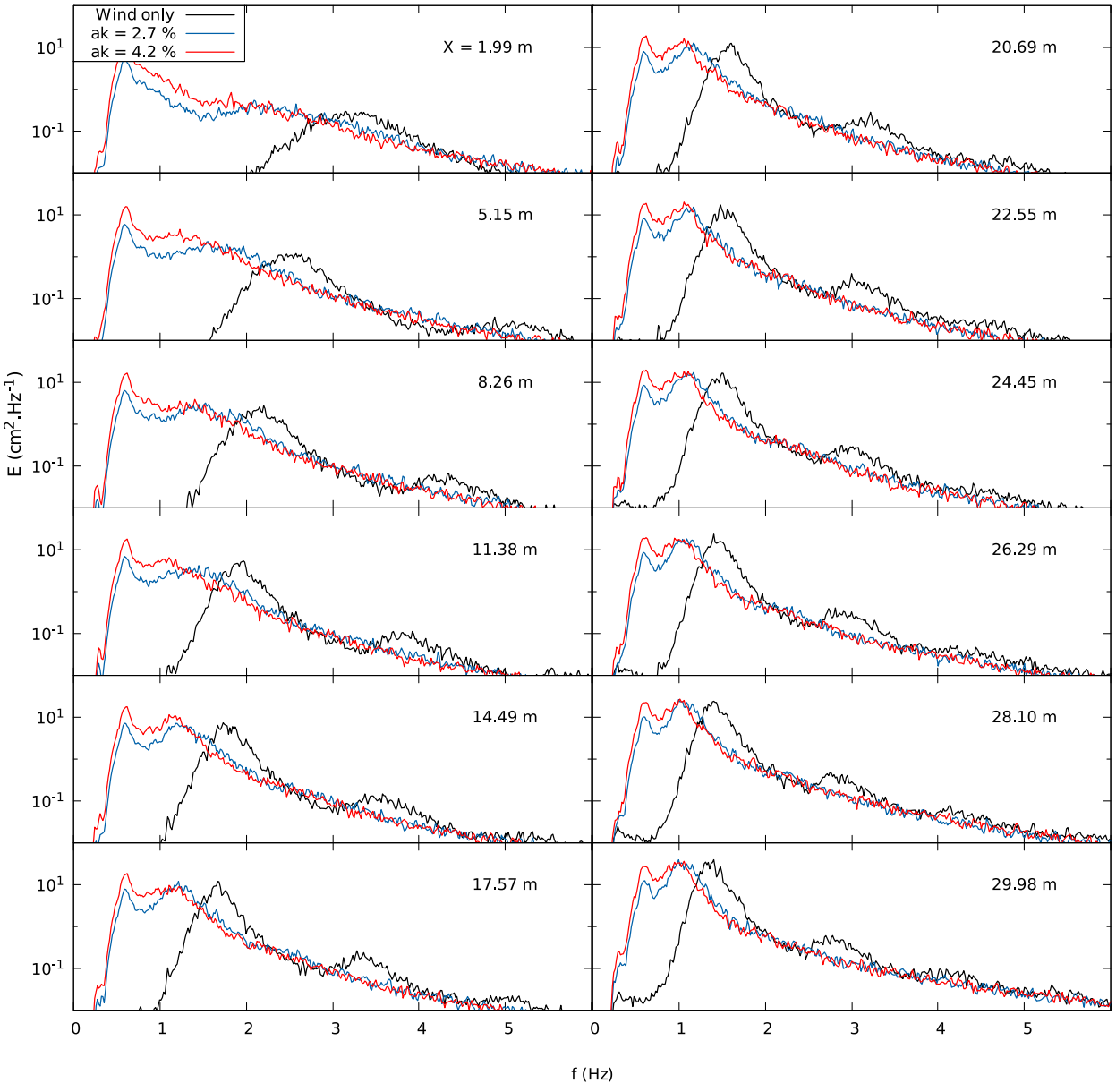


FIG. 11. The spatial evolution of the variance density frequency spectrum with and without irregular paddle waves of steepness $ak$ and peak frequency 0.6 Hz for a wind speed $U_{\mathrm{ref}} = 14\,\mathrm{m\,s^{-1}}$.

increases with the wave amplitude $a$, it appears that the wind-wave steepness is reduced in the presence of paddle waves. Additionally, Fig. 13 shows that the wind-wave steepness is even more lowered when irregular paddle waves are present. This latter observation suggests that nonlinear interactions are a good candidate to explain the slowed decrease of wind wave peak frequency with fetch in the case with irregular waves.

## 7. Extension of the results to the prototype scale

The extent at witch our experimental results, can be generalized at natural scale is discussed in the following. As mentioned in the introduction, the main difference between laboratory and natural scale measurements lies in the wave age of the swell. While the wind velocity conditions produced during the experiment are close to that observed in natural conditions, the mechanically generated waves representing swell are significantly shorter, thus slower, than the swell conditions encountered in the ocean. Thus, an appropriate scaling was performed to compare our experiments with equivalent natural scale observations. Being aware of the main differences in term of wave age, qualitative comparisons permitted to draw tendencies about the physical processes involved in the interaction between swell and wind waves at natural scale.

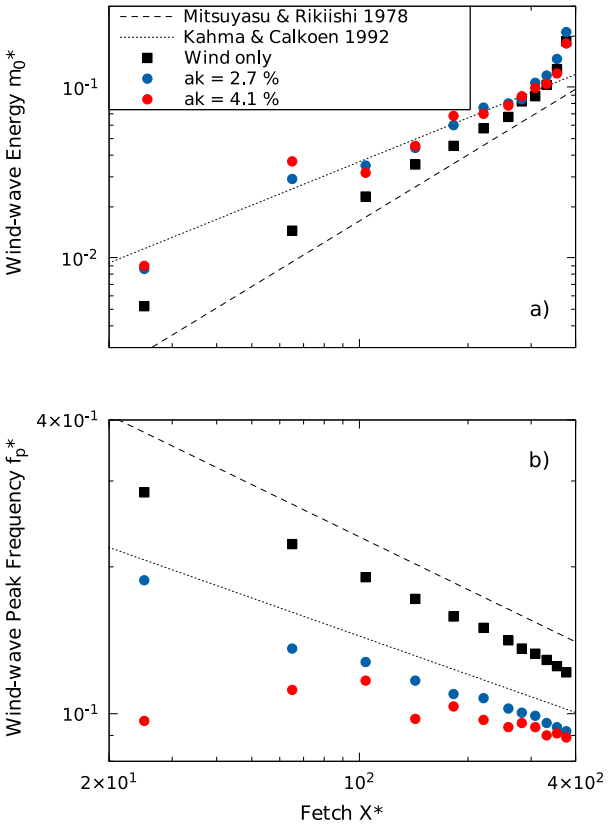


FIG. 12. The spatial evolution of (a) wind-wave energy and (b) peak frequency with and without irregular paddle waves of steepness $ak$ and peak frequency 0.6 Hz for a wind speed $U_{\mathrm{ref}} = 14\,\mathrm{m\,s^{-1}}$.

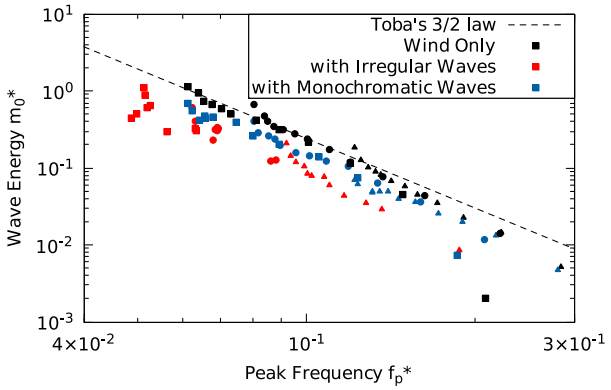


FIG. 13. Variations of the wind waves' dimensionless energy with the dimensionless peak frequency for different reference wind speeds (squares: $U_{\mathrm{ref}} = 6\,\mathrm{m\,s^{-1}}$, circles: $U_{\mathrm{ref}} = 10\,\mathrm{m\,s^{-1}}$, triangles: $U_{\mathrm{ref}} = 14\,\mathrm{m\,s^{-1}}$) compared to variations according to Toba's 3/2 law.

First, an effort was devoted to the determination of the wind friction velocity in order to perform an accurate scaling. Some doubts were formulated regarding the measuring device and the pertinence of the logarithmic profile method to determine the friction velocity in the presence of paddle waves. Using ocean buoy measurements, Vincent et al. (2019) showed that the friction velocity tends to increase with swell steepness especially at low wind speeds. A similar trend is observed in Fig. 5 as the friction velocity increases with the long paddle waves. To confirm the similarities between both scales, it would be necessary to use a method free from the logarithmic profile analogy for the wind profile characterization.

As it was highlighted in section 4, wind-wave growth (without paddle waves) in laboratories shows similarities with that at natural scale. To observe these similarities, laboratory wind waves must be long enough to be free from surface tension effects. Then, the wind-wave energy and peak frequency (Fig. 6) were close to Kahma and Calkoen's empirical relations, representing wind-wave growth at natural scale, but slightly deviated in terms of variations with increasing fetch.

The introduction of paddle waves, representing swell, significantly modifies the wind-wave field. First, monochromatic paddle waves cause a reduction of wind-wave energy. This reduction has received numerous interpretations that reached an agreement on the fact that the physical processes responsible for that reduction are proper to steep short waves (equivalent to paddle waves in natural reservoirs) traveling slower than the wind (i.e., $C \ll U_{10}$). This wind-wave reduction phenomenon was used to design a reduced wind input model for high frequencies waves (i.e., waves with a wave age equivalent to paddle wave) and high winds in Ardhuin et al. (2010). Some gray areas remain on the role played by the monochromatic wave harmonics in the modification of the wind-wave growth. The prominence of these harmonics is principally inherent in laboratory steep monochromatic paddle waves and might damage the relation with wind waves at natural scale.

Second, the wind-wave peak frequency and its variations with increasing fetch are modified in the presence of either irregular or, to a lower extent, monochromatic paddle waves. In Figs. 9b and 12b, the wind-wave peak frequency variations with fetch are closer to Kahma and Calkoen's than to Mitsuyasu and Rikiishi's power laws although the latter is specific for laboratory wind-wave growth. In Table 1, the same tendency can be observed by comparing the power law coefficient $g$ in the presence of paddle waves with the corresponding coefficient in Kahma and Calkoen's law ($g = -0.26$). Furthermore, in the presence of irregular paddle waves, wind-wave energy evolution with increasing fetch follows this agreement with Kahma and Calkoen relations. This accordance can be observed in Fig. 12a or by comparing the power law coefficient $c$ in Table 1 with the coefficient $c = 0.85$ of Kahma and Calkoen. Finally, irregular paddle waves seem to restore wind-wave growth as it is observed at natural scale.

## 8. Conclusions

A series of experiments were carried out at IRPHE–Pythéas wind-wave tank in Marseilles. The interactions between long paddle waves, representing swell, and short wind waves were investigated with both monochromatic and irregular

paddle waves. An analysis was performed in order to identify the interaction mechanisms that can be transposed at prototype scale.

Wind-wave growth was studied in absence of paddle waves to assess the similarities with existing experiments. It was found that, after the young wind waves emancipate from the gravity-capillary state, wind-wave growth is in agreement with laboratory based empirical laws but differ from more general laws (i.e., laws valid at prototype scale) in terms of variations with fetch.

By calculating the vertical profile of the wind horizontal velocity using the logarithmic profile method, the friction velocity had a tendency to increase in the presence of paddle waves. However, the measurements uncertainties added to the limited validity of the logarithmic profile method to characterize the airflow in the presence of long paddle waves prevented a more quantitative analysis. The use of a more accurate method, such as the eddy correlation method, is left for further work.

The interactions between wind and paddle waves have repercussions on the wave systems. The paddle waves are amplified by the wind which echoes back to the sheltering effect highlighted by Chen and Belcher (2000). With monochromatic paddle waves, this shelter effect seems to affect wind-wave growth by reducing the quantity of momentum available for wind-wave generation. In this latter case, the wind mostly impacts the wind-wave energy. Thus, the wind-wave peak frequency evolution with fetch is similar to wind only conditions, resulting in a reduced wind-wave steepness in the presence of monochromatic paddle waves.

The effect of irregular paddle waves on wind-wave growth is quite different since the wind-wave parameter affected by this interaction is mostly the wind-wave peak frequency. The energy continuum brought by the paddle waves high-frequency tail initiates wind-wave growth at a lower frequency than in the absence of paddle waves. Thus, it was found that the irregular low-frequency waves downshift wind-wave peak frequency in a significant manner. The wind-wave energy being only slightly impacted by comparison with the peak-frequency, irregular paddle waves reduces wind-wave steepness even more than in the monochromatic paddle-wave case.

The similarities between the action of monochromatic and irregular paddle waves on wind-wave growth lie in the wind-wave energy and peak frequencies reduced variations with fetch. It is interesting to note that most laboratory measurements, for example, Mitsuyasu and Rikiishi (1978), display an accelerated wind-wave growth (i.e., wind-wave energy increases faster and the peak frequency reduces faster) by comparison with ocean measurements, illustrated here by Kahma and Calkoen's (1992) empirical law. Especially with irregular paddle waves, which is a more faithful reproduction of a typical ocean sea state, wind-wave growth is somehow in accordance with Kahma and Calkoen's (1992) law. A result from this latter observation is that wind-wave growth in laboratories seems closer to wind-wave growth at prototype scale when irregular paddle waves are present.

Finally, our experiments provide a valuable database for validating a spectral wave model. From this database, spectral wave model performances can be assessed under generic conditions for both wind and wave forcing. Using the separation of the physical mechanisms at the root of wind-wave generation in the spectral energy balance equation (1), the ability of the spectral wave model in reproducing wind-wave growth with and without paddle waves might enable to identify the mechanisms at the origin of the wave systems interactions observed in laboratory. Ultimately, the use of a spectral wave model may help to evaluate the extent at which the mechanisms observed in laboratories can be transposed to prototype scale.

*Acknowledgments.* Antoine Villefer acknowledges the financial support of his PhD research program provided by the French ANRT (Association Nationale de la Recherche et de la Technologie) with CIFRE Grant 2019-1257. The authors thank Maria-Joao Teles (EDF R&D LNHE) and Jeffrey Harris (ENPC/LHSV) for many fruitful discussions in the course of this study.

*Data availability statement.* Most of the experimental data collected and analyzed in this article can be obtained upon request from the corresponding author of this article.

## REFERENCES

Ardhuin, F., and Coauthors, 2010: Semiempirical dissipation source functions for ocean waves. Part I: Definition, calibration, and validation. *J. Phys. Oceanogr.*, **40**, 1917–1941, https://doi.org/10.1175/2010JPO4324.1.

Bailey, T., L. Ross, M. Bryant, and D. Bryant, 2020: Predicting wind wave suppression on irregular long waves. *J. Mar. Sci. Eng.*, **8**, 619, https://doi.org/10.3390/jmse8080619.

Benetazzo, A., L. Cavaleri, H. Ma, S. Jiang, F. Bergamasco, W. Jiang, S. Chen, and F. Qiao, 2019: Analysis of the effect of fish oil on wind waves and implications for air–water interaction studies. *Ocean Sci.*, **15**, 725–743, https://doi.org/10.5194/os-15-725-2019.

Cavaleri, L., and Coauthors, 2007: Wave modelling - The state of the art. *Prog. Oceanogr.*, **74**, 603–674, https://doi.org/10.1016/j.pocean.2007.05.005.

Chen, G., and S. E. Belcher, 2000: Effects of long waves on wind-generated waves. *J. Phys. Oceanogr.*, **30**, 2246–2256, https://doi.org/10.1175/1520-0485(2000)030<2246:EOLWOW>2.0.CO;2.

Coantic, M., A. Ramamonjiarisoa, P. Mestayer, F. Resch, and A. Favre, 1981: Wind-water tunnel simulation of small-scale ocean-atmosphere interactions. *J. Geophys. Res.*, **86**, 6607–6626, https://doi.org/10.1029/JC086iC07p06607.

Donelan, M. A., 1987: The effect of swell on the growth of wind waves. *Johns Hopkins APL Tech. Dig.*, **8**, 18–23.

——, W. Drennan, and K. Katsaros, 1997: The air-sea momentum flux in conditions of wind sea and swell. *J. Phys. Oceanogr.*, **27**, 2087–2099, https://doi.org/10.1175/1520-0485(1997)027<2087:TASMFI>2.0.CO;2.

——, B. K. Haus, W. J. Plant, and O. Troianowski, 2010: Modulation of short wind waves by long waves. *J. Geophys. Res.*, **115**, C10003, https://doi.org/10.1029/2009JC005794.

Dorn, W. G. V., 1966: Boundary dissipation of oscillatory waves. *J. Fluid Mech.*, **24**, 769–779, https://doi.org/10.1017/S0022112066000995.

Hasselmann, K., 1962: On the non-linear energy transfer in a gravity-wave spectrum Part 1. General theory. *J. Fluid Mech.*, **12**, 481–500, https://doi.org/10.1017/S0022112062000373.

——, and Coauthors, 1973: Measurements of wind-wave growth and swell decay during the Joint North Sea Wave Project (JONSWAP). *Deut. Hydrogr. Z.*, **8**, 1–95.

Hwang, P. A., H. García-Nava, and F. J. Ocampo-Torres, 2011: Observations of wind wave development in mixed seas and unsteady wind forcing. *J. Phys. Oceanogr.*, **41**, 2343–2362, https://doi.org/10.1175/JPO-D-11-044.1.

Janssen, P. A. E. M., 2004: *The Interaction of Ocean Waves and Wind*. Cambridge University Press, 312 pp.

Kahma, K. K., and C. J. Calkoen, 1992: Reconciling discrepancies in the observed growth of wind-generated waves. *J. Phys. Oceanogr.*, **22**, 1389–1405, https://doi.org/10.1175/1520-0485(1992)022<1389:RDITOG>2.0.CO;2.

Kitaigorodskii, S., 1961: Application of the theory of similarity to the analysis of wind generated wave motion as a stochastic process. *Izv. Akad. Nauk SSSR, Ser. Geofiz.*, **1**, 105–117, https://doi.org/10.1016/0011-7471(62)90050-5.

Komen, G. J., L. Cavaleri, M. Donelan, K. Hasselmann, S. Hasselmann, and P. A. E. M. Janssen, 1994: *Dynamics and Modelling of Ocean Waves*. Cambridge University Press, 556 pp.

Mackay, E., 2011: Modelling and description of omnidirectional wave spectra. *Proc. 9th European Wave and Tidal Energy Conf. (EWTEC 2011)*, University of Southampton, Southampton, United Kingdom, 122–131.

Masson, D., 1993: On the nonlinear coupling between swell and wind waves. *J. Phys. Oceanogr.*, **23**, 1249–1258, https://doi.org/10.1175/1520-0485(1993)023<1249:OTNCBS>2.0.CO;2.

Miles, J. W., 1957: On the generation of surface waves by shear flows. *J. Fluid Mech.*, **3**, 185–204, https://doi.org/10.1017/S0022112057000567.

Mitsuyasu, H., 1966: Interactions between water waves and wind (1). *Rep. Inst. Appl. Mech. Kyushu Univ.*, **14**, 67–88.

——, and K. Rikiishi, 1978: The growth of duration-limited wind waves. *J. Fluid Mech.*, **85**, 705–730, https://doi.org/10.1017/S0022112078000889.

——, and Y. Yoshida, 1991: The effect of swell on the growth of wind waves. *Elsevier Oceanogr. Ser.*, **54**, 381–392, https://doi.org/10.1016/S0422-9894(08)70110-7.

Monin, A. S., and A. M. Obukhov, 1954: Basic laws of turbulent mixing in the surface layer of the atmosphere. *Tr. Geofiz. Inst., Akad. Nauk SSSR*, **24**, 163–187.

Phillips, O. M., and M. L. Banner, 1974: Wave breaking in the presence of wind drift and swell. *J. Fluid Mech.*, **66**, 625–640, https://doi.org/10.1017/S0022112074000413.

Shemer, L., 2019: On evolution of young wind waves in time and space. *Atmosphere*, **10**, 562, https://doi.org/10.3390/atmos10090562.

Toba, Y., 1997: The 3/2-power law for ocean wind waves and its applications. *Advances in Coastal and Ocean Engineering*, Vol. 3, P. L.-F. Liu, Ed., World Scientific, 31–65, https://doi.org/10.1142/9789812797568_0002.

Vincent, C. L., J. Thomson, H. C. Graber, and C. O. Collins III, 2019: Impact of swell on the wind-sea and resulting modulation of stress. *Prog. Oceanogr.*, **178**, 102164, https://doi.org/10.1016/j.pocean.2019.102164.

Welch, P., 1967: The use of fast Fourier transform for the estimation of power spectra: A method based on time averaging over short, modified periodograms. *IEEE Trans. Audio Electroacoust.*, **15**, 70–73, https://doi.org/10.1109/TAU.1967.1161901.

Wright, J. W., 1976: The wind drift and wave breaking. *J. Phys. Oceanogr.*, **6**, 402–405, https://doi.org/10.1175/1520-0485(1976)006<0402:TWDAWB>2.0.CO;2.